ORIGINAL PAPER

Asymmetric Thioethers as Building Blocks for Chiral Monolayers

**April D. Jewell · Heather L. Tierney ·
Oussama Zenasni · T. Randall Lee ·
E. Charles H. Sykes**

Abstract There is a growing interest in chirality at surfaces from both a fundamental and an enantioselective reactions/separations viewpoint. We report on the homochiral self-assembly of asymmetric thioethers that become chiral upon binding to a surface. We focus on the adsorption of butyl methyl sulfide and a fluorinated analogue on Au(111) surfaces.

Keywords Chirality · Self-assembly · Dipole moment · Scanning tunneling microscopy · Thioether

1 Introduction

In the mid-nineteenth century, Louis Pasteur performed the first experiments that provided direct evidence of chirality on the molecular scale [1]. Since then, researchers have taken advantage of molecular chirality in a variety of fields and applications. Self-assembled monolayers of chiral molecules have proven to be very useful systems for the study of two-dimensional chiral interactions, separations, templating, and amplification. In the arena of chiral assembly, tartaric acid [2–10], cinchona alkaloids [11–13]

A. D. Jewell · H. L. Tierney · E. C. H. Sykes (✉)
Department of Chemistry, Tufts University, 62 Talbot Avenue,
Medford, MA 02155, USA
e-mail: Charles.Sykes@tufts.edu

O. Zenasni · T. R. Lee
Department of Chemistry and the Texas Center for
Superconductivity, University of Houston, 4800 Calhoun Road,
Houston, TX 77204-5003, USA

and heptahelicene [14–16] are among the most commonly studied molecules. Several reports in the literature have revealed that chiral adlayers on achiral surfaces exhibit enantiospecific interactions with chiral probe molecules [17–20]. For example, (S)-propylene oxide exhibits a preference for adsorption on a Pt(111) surface modified with (S)-butoxide over an identical surface modified with (R)-butoxide, with the former system adsorbing 35% more of the probe molecule than the latter [18].

Applications of self-assembled monolayers (SAMs) often take advantage of tunable chemical functionality and shape. For example, the most common type of SAM involves thiol species (HSR) and utilizes a strong sulfur-metal interaction to form the layers [21–25]. Thiols can be functionalized with groups that are polar, aromatic, etc. Typically, the formation of chiral adlayers has relied on the self-assembly of species that are chiral in the gas phase [2–4, 17, 18, 20, 26, 27] or that organize into rigid structures via hydrogen-bonding interactions [28–39]. However, some molecules that are achiral in the gas phase can exhibit a surface-bound chirality due to the removal of mirror symmetry [29, 35, 40]. The adlayers formed from such prochiral species are necessarily racemic in nature. However, Ernst and Raval have demonstrated that the use of a chiral perturbation, or a small percentage of a "seed molecule", can flip the chirality of the adsorbed molecules, thus creating an overall single-handed organization [9, 10, 14, 41].

In this paper, we extend our previous work on symmetric thioether (RSR) self-assembly [42–44] to asymmetric thioethers (RSR′) and show that these monolayers are chiral by virtue of the binding of one of the two pro-chiral lone pairs on the S atom to the Au surface [45]. We find that well-ordered domains of butyl methyl sulfide (BMS) and 4,4,4-trifluorobutyl methyl sulfide (4TF-BMS) form due to van der Waals interactions between molecules, and that the self-

assembly is almost 100% enantiospecific, leading to the growth of large homochiral domains. With future applications in mind, we also present a study of a partially fluorinated asymmetric thioether and show that despite this substitution, the same highly enantiospecific assembly leads to similar, well-ordered homochiral domains. We hope to eventually use these chiral, dipolar layers for studies of spin-polarized electron transmission through organic layers. Also, the fact that asymmetric thioethers are pro-chiral in the gas phase but form enantiomorphic domains when surface-adsorbed offers possibilities for the interrogation of chirality at surfaces. Such experiments might involve symmetry breaking, in which small amounts of a chiral "seed" species are introduced to amplify the global single-handed organization of the molecules.

2 Methods and Materials

2.1 Low-Temperature Scanning Tunneling Microscopy

All scanning tunneling microscopy (STM) experiments were performed in a low-temperature, ultrahigh vacuum (LT-UHV) microscope built by OmicronNanotechnology™. The Au(111) sample was purchased from MaTecK. Two cycles of Ar^+ sputtering (1.0 keV/14 μA) for 30 min followed by 15 min anneal periods up to 1000 K were performed between each STM experiment. After the final anneal, the crystal was transferred in less than 5 min in vacuum ($<5 \times 10^{-10}$ mbar) into the pre-cooled STM. In approximately 30 min, the sample cooled from room temperature to 78 K. All images were recorded at 78 K with etched W or Ni tips, and voltages refer to the sample bias. Low-temperature (<300 K) annealing treatments were performed by removing the sample from the STM stage and placing it into a sample holder room temperature at the edge of the STM UHV chamber. The temperatures attained using this procedure were determined by the total anneal time and were calculated from thermal diffusion studies of dimethyl sulfide on Cu(111) [42, 43]. For both species under investigation, molecular coverage values were calculated from molecularly resolved STM images; one monolayer (ML) refers to full coverage with a $(\sqrt{13} \times \sqrt{3})R13.9^{\circ}$ unit cell. Herringbone reconstruction measurements, which can be used to indicate molecule-surface interaction strength, were performed using large-scale STM images and represent the average herringbone separation measured perpendicular to the soliton walls.

2.2 Butyl Methyl Sulfide Preparation

Butyl methyl sulfide (BMS) was obtained from the rare chemical library of Sigma-Aldrich and was further purified by cycles of freeze/pump/thaw prior to introduction to the STM chamber via a precision leak valve. The purity of the BMS sample has been previously determined by experiment to be >99% from both high-resolution STM and mass spectrometry data [46]. BMS was deposited from the liquid state onto the cold sample (78 K) by a collimated molecular doser.

2.3 4,4,4-Trifluorobutyl Methyl Sulfide Synthesis and Preparation

4,4,4-Trifluorobutyl methyl sulfide (4FT-BMS) is not commercially available, and was prepared via a novel synthetic approach. 1-Bromo-4,4,4-trifluorobutane was purchased from Oakwood Inc., and sodium thiomethoxide was purchased from Sigma-Aldrich. All solvents were used as purchased unless otherwise stated. In a 250 mL three-necked round-bottomed flask equipped with an addition funnel and a reflux condenser, 1-bromo-4,4,4-trifluorobutane (2.0 g, 10 mmol) was dissolved in 50 mL of anhydrous methanol under argon atmosphere. Sodium thiomethoxide (1.5 g, 21 mmol) was dissolved in methanol (previously degassed), and was added drop-wise to the stirred solution of the bromide over 15 min. The mixture was refluxed for 8 h. After cooling to room temperature, the reaction was quenched using 50 mL of water. The mixture was extracted with 3×75 mL of diethyl ether. The organic layer was washed with 50 mL of brine and dried over $MgSO_4$. The solvent was removed by rotary evaporation, and the residue was dried under vacuum. The residue was then dissolved in 30 mL of dry diethyl ether and added to a stirred suspension of $LiAlH_4$ (0.20 g, 6.3 mmol) in 15 mL of diethyl ether at -5 °C. The reaction was stirred at RT for 6 h under argon. The mixture was then cooled to -5 °C and quenched with 50 mL of water. Aliquots of a 1 M aqueous HCl solution were added until the aqueous layer became acidic as indicated by litmus paper. The resulting mixture was extracted with diethyl ether (3×50 mL). The organic layers were combined and washed with brine (50 mL), dried with $MgSO_4$, and filtered. The solvent was removed by rotary evaporation. The product was purified by distillation under vacuum; the fraction collected at -50 °C at 500 millitorr gave 4TF-BMS in 48% yield from the starting bromide. The purity of the sample was confirmed to be >95% with ^{1}H NMR (400 MHz, $CDCl_3$) and ^{13}C NMR (125 MHz, $CDCl_3$) spectroscopies as well as GC/MS (see Supplemental Information for spectra). 4TF-BMS was further purified by cycles of freeze/pump/thaw prior to introduction to the STM chamber via a leak valve and was deposited from the liquid state onto the cold sample (78 K) by a collimated molecular doser.

3 Results and Discussion

3.1 Self-Assembly of Asymmetric Thioethers

Previous reports have shown that symmetric thioethers (RSR) adsorbed intact on a Au(111) surface with their alkyl tails parallel or nearly-parallel to the substrate [43, 44, 47–52]. The molecules bonded through one of the two lone pairs on the central S atom and maintained their tetrahedral geometry in the adsorbed state [45]. Furthermore, RSR species formed well-ordered arrays built of rows of molecules with their S atoms aligned and alkyl tails parallel to one another, held together by van der Waals interactions between the alkyl tails [43, 44, 49–51].

Figure 1 shows the nanometer-scale characteristics for the long-range self-assembly of butyl methyl sulfide (BMS) on Au(111). BMS is an asymmetric thioether species (see schematic in Fig. 1a). When adsorbed on Au(111), BMS forms self-assembled systems that vary as a function of coverage. At low-coverage (<0.3 ML), BMS molecules show no preference for any region of the Au surface and essentially stick where they land, as shown in Fig. 1a. Upon further adsorption, BMS exhibits no long-range ordering at 78 K. The system was then annealed to 120 K, after which the molecules aggregate into well-ordered rows. This observation suggests that long-range ordering is a kinetically-limited process that requires thermal diffusion of the molecules [44]. At medium coverage (0.3 to 0.8 ML), after annealing to 120 K, BMS forms small domains of ordered rows of molecules. A representative image of BMS at medium coverage is shown in Fig. 1b. The sizes and shapes of the molecular domains are dictated by the soliton walls of gold's reconstruction, which separate fcc and hcp stacked regions of the surface and appear as pairs of lines running along the surface. Adsorbed molecules exhibit different binding preferences for the different regions of the Au surface, with molecules aggregating first in the wider

fcc-packed regions, then the narrower hcp-packed regions, and finally the soliton regions of the surface reconstruction. This variation in stability within the different regions of the surface suggests a preference for adsorption in fcc areas either due to the atomic spacing or local electronic structure [53–57]. At high coverage (>0.9 ML), the molecules form large continuous domains that span all regions of the herringbone reconstruction.

4TF-BMS was designed and synthesized to be a highly dipolar analog of BMS, with three fluorine atoms at the end of the butyl tail (see schematic in Fig. 2a). Even with this added functionality, 4TF-BMS shows similar self-assembly properties to BMS at low, medium, and high coverage (Fig. 2). The medium- and high-coverage systems of 4TF-BMS were also annealed to 120 K to promote long-range molecular assembly before imaging at 78 K. Furthermore, the 4TF-BMS shows the same regional preferences as its non-fluorinated counterpart, being most likely to aggregate in the fcc-, then hcp-, then soliton regions of the Au surface.

Higher-resolution, molecularly resolved STM images allowed for the determination of local molecular packing. The images in Fig. 3 reveal that both BMS and 4TF-BMS adsorb intact with their alkyl tails parallel or nearly parallel with the Au substrate. Both species exhibit a $(\sqrt{13} \times \sqrt{3})$ R13.9° unit cell as shown in Fig. 3. The herringbone reconstruction is removed with increasing molecular coverage and temperature treatments (this phenomenon will be explored in detail in Sect. 3.3). As such, the majority of the molecular domains reside on 1×1, unreconstructed Au(111); therefore, the $(\sqrt{13} \times \sqrt{3})$ unit cell describes the periodicity of the molecular overlayer with respect to the ideal (i.e., unreconstructed) Au(111) surface with a Au–Au spacing of 0.288 nm.

Our previous studies examining dimethyl sulfide (DMS) and dibutyl sulfide (DBS) on Cu(111) and Au(111) offer evidence that van der Waals attractions play an important role in the assembly of the longer tailed species [42–44, 58].
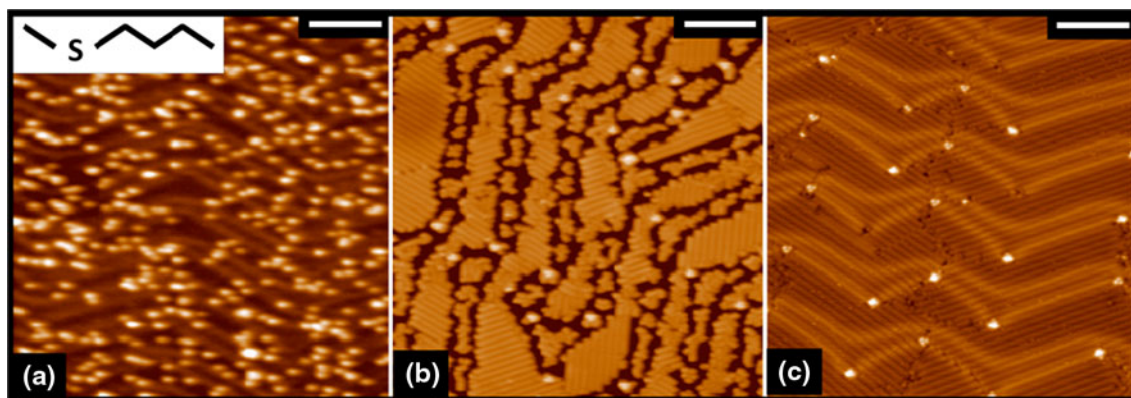

Fig. 1 STM images showing **a** 0.19 ML, **b** 0.67 ML, and **c** 0.99 ML BMS on Au(111). The low-coverage system in (**a**) was imaged as dosed at 78 K, while the medium and high systems in (**b**) and (**c**), respectively, were annealed to 120 K prior to imaging at 78 K. *Scale bars* 10 nm. Imaging conditions: 78 K; **a** & **b** 10 pA, 100 mV. **c** 200 pA, 200 mV
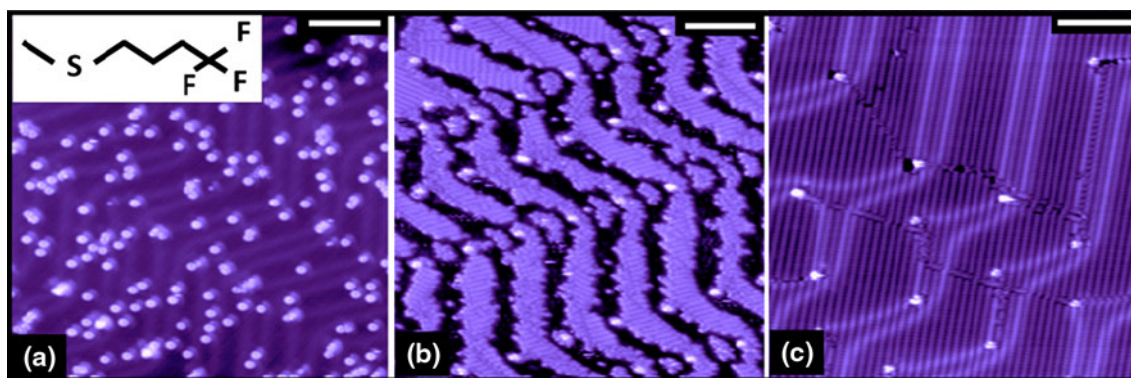
Fig. 2 STM images showing **a** 0.18 ML, **b** 0.63 ML, and **c** 0.99 ML 4FT-BMS on Au(111). The low-coverage system in (**a**) was imaged as dosed at 78 K, while the medium- and high-coverage systems in (**b**) and (**c**), respectively, were annealed to 120 K prior to imaging at 78 K. *Scale bars* 10 nm. Imaging conditions: 78 K; **a** 100 pA, −300 mV. **b** 100 pA, 600 mV. **c** 500 pA, −500 mV
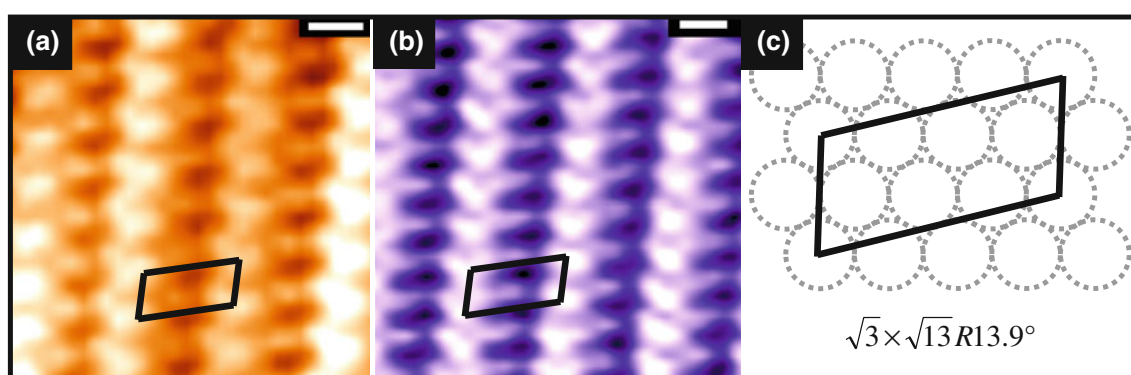

$$\sqrt{3} \times \sqrt{13}\, R13.9°$$

Fig. 3 Molecularly-resolved STM images showing the unit cell packing structure of **a** BMS, and **b** 4TF-BMS on Au(111). The schematic in (**c**) shows the unit cell dimensions with respect to the underlying atomic lattice. *Scale bars* 0.5 nm. Imaging Conditions: 78 K; **a** 200 pA, 200 mV. **b** 300 pA, −600 mV

DMS arranges in a perpendicular (or "herringbone") packing arrangement, which is typical of quadrupolar molecules [42, 58]. However, DBS, which is very chemically similar to DMS, packs in linear rows [43, 44]. The difference in packing structure of the two molecules is due to the competition between intermolecular quadrupole–quadrupole and van der Waals interactions. DMS has short alkyl chains, and quadrupole–quadrupole interactions dominate the packing energetics, leading to a herringbone packing structure. DBS, however, has larger alkyl chains that contribute to increased van der Waals interactions. This interaction is larger than the quadrupole–quadrupole energy and forces the molecules to arrange in linear chains that maximize van der Waals interactions.

Additionally, density functional theory (DFT) charge calculations for the adsorption of BMS on Au show that upon adsorption, a charge of 0.11 e^- is transferred to the surface from the S atom of the molecule [59]. Thus, there is a partial positive charge on the S atom, and a corresponding partial negative charge on the metal surface beneath. From the perspective of electrostatics, it would be unfavorable for the S atoms to align in straight rows;

however, this behavior is observed. It is likely that the same competing quadrupole–quadrupole and van der Waals interactions discussed above are at play in determining the packing structure for BMS and 4FT-BMS.

The fact that BMS and 4FT-BMS self-assemble on Au(111) in a similar manner indicates that substitution of three H atoms for F atoms does not significantly alter the molecular packing structure. The difference between the van der Waals radii of the C–H and C–F bond is ∼0.02 nm, or 4% of the average thioether–thioether molecule spacing of 0.5 nm [60]. This means that, in steric terms, the BMS and 4FT-BMS molecules are almost identical. Also, our previous work exploring DBS SAM formation on Au(111) revealed that the majority of the molecular rows (94%) ran predominantly in the two partially compressed [11$\bar{2}$] directions [44]. These finding suggest that the DBS molecules are electrostatically stable even with the slightly closer separation (0.482 vs. 0.499 nm) exhibited by this lattice direction. Furthermore, as previously discussed, the monolayer structure of BMS is in part driven by van der Waals interactions. Due to electron pair donation to the surface, the S atom of each molecule has a partial positive charge [59]. The F atoms

at the end of each butyl tail in 4FT-BMS are strongly electron withdrawing, resulting in a partial negative charge. As such, we can describe the 4FT-BMS molecular rows as being a series of nested dipolar molecules. Therefore, from both a size and electrostatics perspective BMS and 4TF-BMS are most stable in the same molecular arrangements.

3.2 Homochiral Domain Formation

Within the islands of self-assembled BMS and 4TF-BMS that form at medium to high coverage, there are a few domain boundaries. Figure 4 shows a high-resolution image of 0.83 ML of 4TF-BMS; upon close inspection, it is clear that boundaries separate homochiral domains of the molecules. When these molecules (which are achiral in the gas phase) adsorb on a surface, bonding occurs through only one of the two pro-chiral lone pairs on the S atom [45, 59]. The alkyl tails align parallel to the surface; thus, the thioether molecules essentially retain their tetrahedral geometry upon adsorption [45]. This bonding behavior leads to two surface-bound enantiomers depending on which of the lone pairs bonded to the surface (see Fig. 4 for schematic) [59]. In STM images, the adsorbed molecules appear as "V-shaped" protrusions, with one leg of the V shorter than the other, corresponding to the methyl group. Thus, the chirality of the adsorbed molecules can be inferred based on their appearance in STM images.

Due to the three-fold symmetry of the hexagonally packed Au(111) surface and the asymmetry of the molecules, the molecular domains can adopt one of 12 orientations (see Fig. 5 for schematic). Due to a 180° rotation about each close-packed lattice direction, each row of molecules can orient with its tails pointing up or down relative to each atomic row. Therefore, six different rotational positions can exist for molecular rows of a single enantiomer [45–47, 52, 61, 62]. As there are two enantiomers, there is the possibility for the assembly of 12 monolayer structures on the surface, each related by rotational or mirror symmetry. Each of these twelve structures has the same ($\sqrt{13} \times \sqrt{3}$) unit cell, with a rotation of $+13.9°$ (clockwise) for the S enantiomers and $-13.9°$ (anti-clockwise) for the R enantiomers. Thus, the images and schematic in Fig. 3 show domains and the unit cells of R enantiomers for both BMS and 4TF-BMS. Figure 5 shows STM images of 4TF-BMS with corresponding unit cell schematics for each of the twelve possible orientations. All 12 of these domains were found on self-assembled monolayers of both BMS and 4TF-BMS. See the Supplemental Information for a similar figure for BMS.

Our previous study using DFT calculations showed that the R and S surface-bound enantiomers of BMS are equivalent in energy, as would be expected [59]. Thus, there is no preference for adsorption in either configuration.
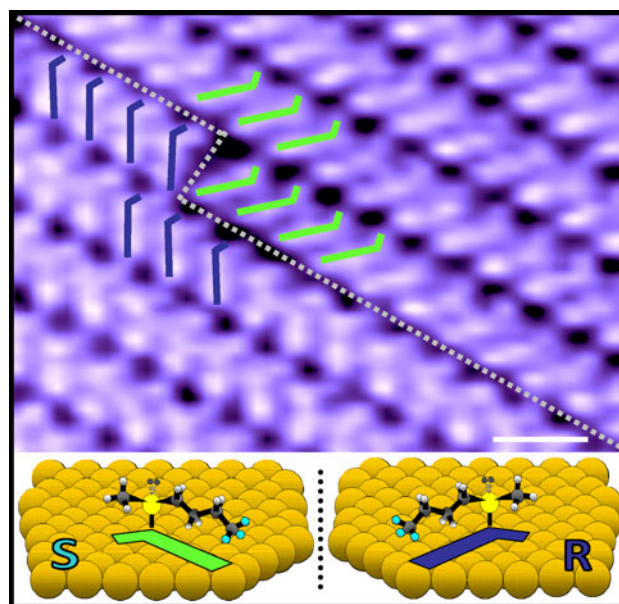

Fig. 4 STM image (*top*) showing the boundary between two homochiral domains in a 4TF-BMS system. These molecules are achiral in the gas phase, but become chiral when adsorbed on a surface. The schematics in the lower portion of the figure show the mirror symmetry of two adsorbed asymmetric thioether species. The handedness (*R* vs. *S*) of the surface-bound molecule is determined by which lone pair interacts with the surface. In the schematic, the surface is comprised of Au (gold) atoms; S is *yellow*, C is *black*, H is *white*, and F is *cyan*. *Scale bar* 1 nm. Imaging conditions: 78 K, 300 pA, 600 mV

DFT calculations also revealed that the barrier to invert from one enantiomer to the other, which requires switching the lone pair bound to the surface, is on the order of 0.24 eV [59]. Assuming the inversion exhibits Arrhenius-type behavior with a typical pre-factor $\sim 10^{12}$, at 78 K (the sample temperature during deposition) the molecules invert chirality at a rate of ~ 0.0001 Hz. At 120 K (the annealing temperature that led to the formation of large homochiral domains), the inversion rate would be ~ 80 Hz.

Previous reports of the self-assembly of dibutyl sulfide (DBS) on Au(111) showed that symmetric thioether molecules diffused on the surface at a rate that increased with temperature [44]. When the molecules diffused to within a nanometer of each other, they interacted to form chains [44]. A similar process of diffusion and self-assembly likely occurs in the asymmetric thioether systems as well. The equal and random distribution of R and S enantiomers coupled with the rapid inversion of chirality at elevated temperatures (~ 80 Hz at 120 K) dictate that the number of (R–R), (S–S), and (R–S) collisions are nearly equivalent. If all molecule–molecule interactions were also equivalent, then one would expect to see a predominance of disordered, heterochiral domains. The fact that we observe ordered, homochiral domains almost exclusively suggests that (R–R) and (S–S) molecular interactions are
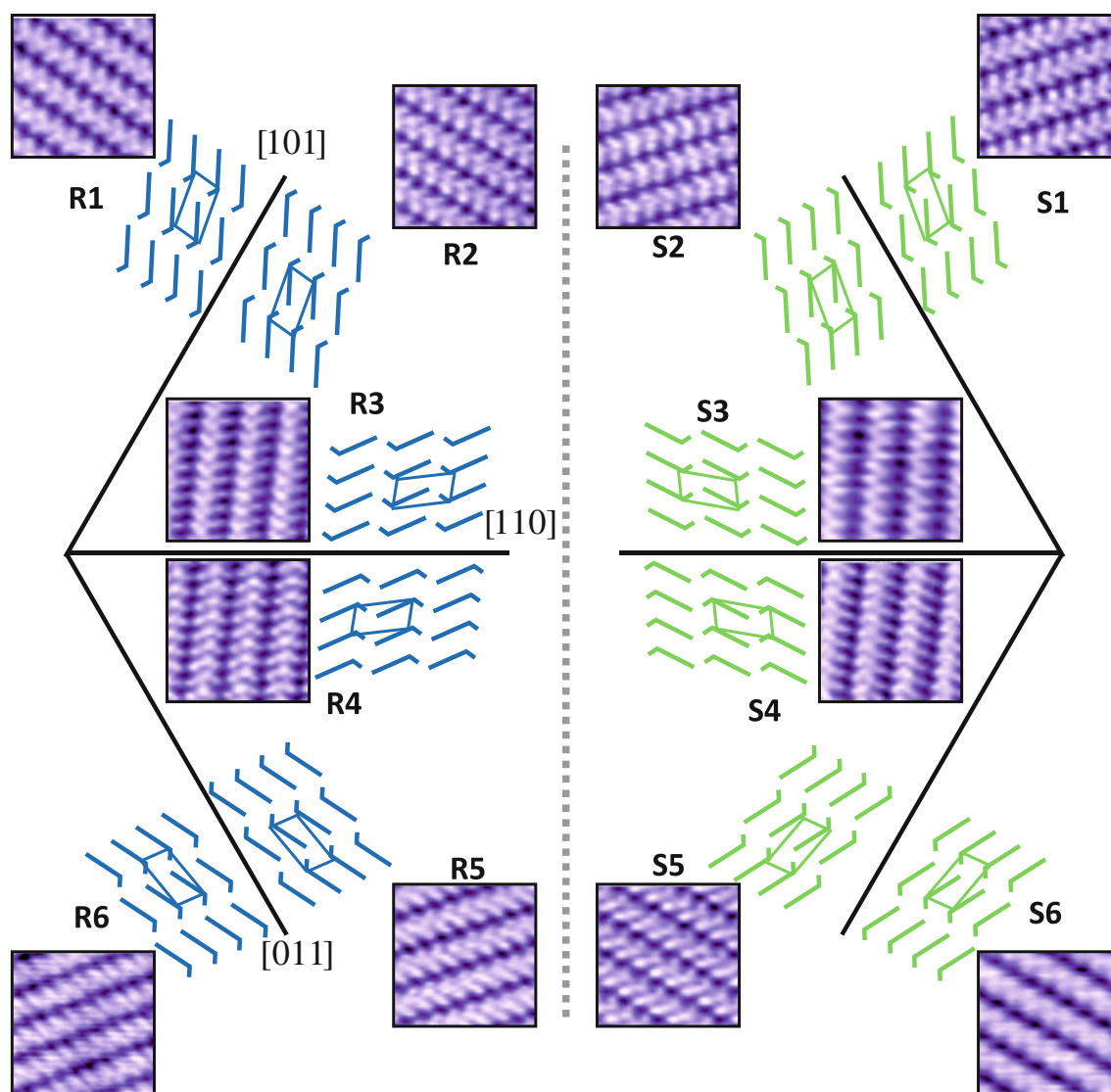
Fig. 5 STM images and schematics showing the 12 molecular packing structures for 4TF-BMS on Au(111). Six of the orientations arise for each of the molecule's two enantiomers due to the three-fold symmetry of the (111) surface lattice. All 12 structures are related by either rotational or mirror symmetry. S/R labels refer to the different rotational domains for the packing of the two enantiomers. All images are ∼4 nm × 4 nm in dimension. Imaging conditions: 78 K, 10–500 pA, ± (100–600) mV

energetically favorable compared to (*R–S*) interactions. This result is consistent with the fact that van der Waals interactions between the alkyl tails stabilize the layers; the nested butyl–butyl/methyl–methyl interaction in homochiral pairs is more stable than the butyl–methyl/methyl–butyl interaction of heterochiral (*R–S*) pairs.

At 120 K (the lowest anneal temperature used in this investigation), molecules on the surface diffuse and invert their chirality rapidly. The process of homochiral domain formation can occur via two routes. When similar enantiomers (*R–0* or *S–S*) collide, the chains formed would be relatively stable. However, if dissimilar enantiomers (*R–S*) collide, the resultant chains would be less stable. In the first proposed mechanism, the dissimilar enantiomers stay together for only a short time before separating and diffusing to find like molecules with which to interact. In the second mechanism, the two dissimilar enantiomers undergo rapid inversion until their chiralities match, stabilizing the resulting chain. Assuming that both processes occur on similar timescales, it is likely that both mechanisms contribute to the process of homochiral domain formation. Time-lapse imaging experiments are currently underway to determine if either mechanism dominates and whether the chirality inversion is distance-dependent.

At this point, it is important to mention the effect of the gold substrate's native reconstruction on molecular

Fig. 6 STM images of medium (*top*) and high (*bottom*) coverage BMS (*left*) and 4TF-BMS (*right*) on Au(111). At medium coverage, small homochiral domains are formed in both systems. The domains are primarily confined to the fcc-regions of the Au surface. At high coverage, homochiral domains span across the herringbones to form large ($>10^3$ nm^2) domains. *Scale bars* 5 nm. Imaging conditions: 78 K; **a**, **b** 200 pA, 200 mV. **c** 300 pA, −600 mV. **d** 500 pA, −500 mV
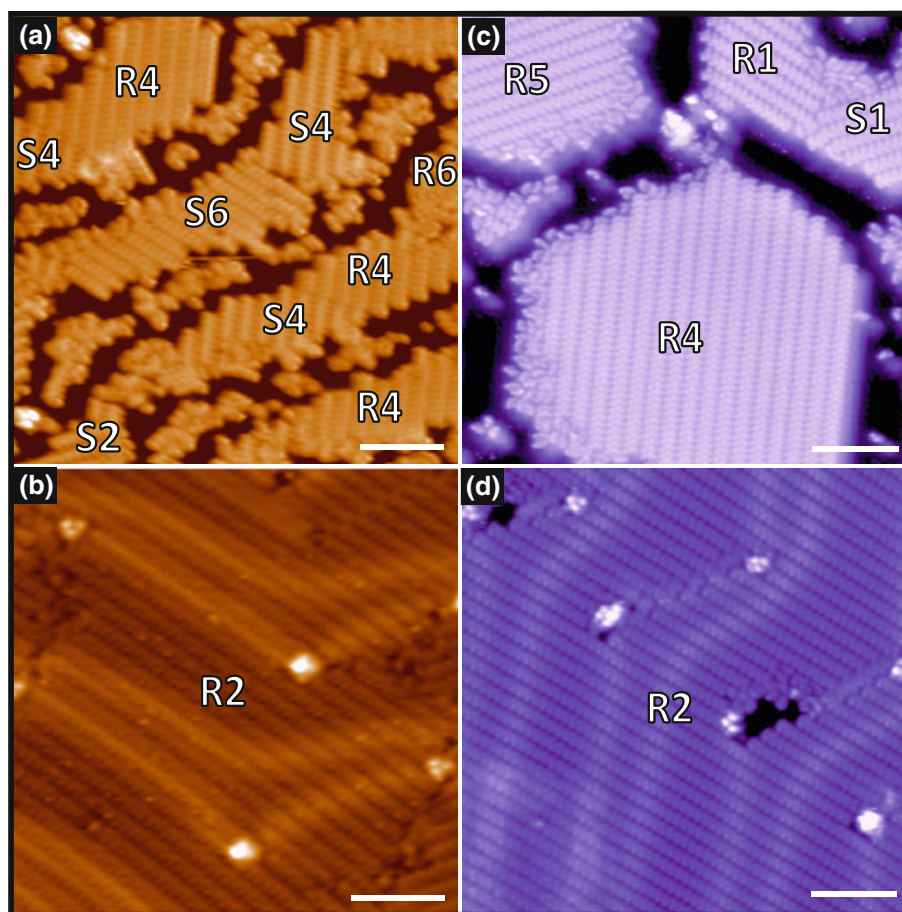
assembly. At medium coverage, the boundaries of the molecular domains are determined by the directionality of the herringbone reconstruction. At near monolayer coverage, however, the molecular layer crosses the soliton walls of the herringbone reconstruction, creating large homochiral domains that are seemingly unaffected by the gold surface. Both of these effects can be seen in Figs. 1 and 2. While equivalent numbers of each enantiomeric domain are found, each of the homochiral domains can span areas on the order of 10^3–10^4 nm^2 (see Fig. 6 for comparisons). Thus, this system provides control over the size of enantiopure domains based solely on the coverage of the system.

Although there are large homochiral domains in our systems, the overall architecture is racemic in nature. This global achirality is similar to that observed for 50:50 (R,R)-tartaric acid: (S,S)-tartaric acid adsorbed on Cu(110) [2]. Subsequent experiments with tartaric acid have shown that using a slight enantiomeric excess can lead to systems displaying a predominance of single-handed organization. In these non-racemic tartaric acid systems, the minor component often displayed a tendency to remain disordered on the surface [2].

Given that the molecules used in this study are achiral in the gas phase, it is not feasible to break symmetry by introducing an initial enantiomeric excess. However, it might be possible to take advantage of the molecules' ability to interconvert between its two energetically equivalent enantiomers. Future plans include using the approach of finding appropriate seed molecules for these thioether systems [9, 10, 14].

3.3 Surface Interaction: Lifting Gold's Herringbone Reconstruction

Adsorbates with a weak interaction with Au(111), such as styrene ($\sim$60 kJ/mol), do not lift the herringbone reconstruction [63]. However, adsorbates with a stronger interaction with Au(111), such as thiols ($\sim$130 kJ/mol), fully lift the herringbone reconstruction to form (1 × 1) Au [21–24, 54, 64]. Bellisario et al. [44] showed that the adsorption of the symmetric thioether species DBS caused gold's native herringbone reconstruction to be *partially* lifted, even at temperatures as low as 120 K. Temperature programmed desorption experiments have indicated that the DBS gold interaction is $\sim$90 kJ/mol [24]. As a measure of the interaction strength of thioethers with Au surfaces, we use the spacing of the herringbone reconstruction [65]. A weakly interacting molecule does not alter the surface, and

hence the spacing remains at 6.3 nm, the unit cell of clean Au $(22 \times \sqrt{3})$. Slightly stronger interacting adsorbates remove a few atoms from the surface, thereby annihilating some of the herringbones and making their separation appear larger. After the extra 4.5% surface Au atoms are removed, the herringbones disappear completely, and their spacing is infinite. As herringbone spacing can be easily measured from STM images, this approach provides an accurate measure of the interaction strength of adsorbates as a function of coverage and molecular chemistry [44, 65].

Figure 7 shows the herringbone spacing as a function of BMS and 4TF-BMS coverage. These systems were annealed to 120 K following each subsequent dose. As the BMS coverage increases (orange), the herringbone spacing remains relatively unchanged; however, as 4TF-BMS coverage increases (purple), the herringbone spacing increases slightly. The data therefore suggest a slightly stronger interaction between Au and the partially fluorinated thioether than with the unfluorinated analog. The variability in the herringbone spacing as a function of molecular coverage can be seen in the STM images in Figs. 1, 2 and 6.

The full coverage BMS and 4TF-BMS systems (shown in Figs. 1c, 2c, respectively) were also annealed to successively higher temperatures from 120 to 220 K. The herringbone spacing is presented as a function of annealing temperature in Fig. 8. As the temperature increases, some of the molecules desorb, leading to lower coverage as indicated by the numbers (% of ML) on the bars in Fig. 8. The data reveal that 120 K is sufficiently hot enough to promote a restructuring of the Au surface, as indicated by the slight increase in the herringbone separation. A subsequent anneal at 160 K is enough to promote a marked increase in the herringbone separation, indicating a significant restructuring of the Au surface. Further annealing
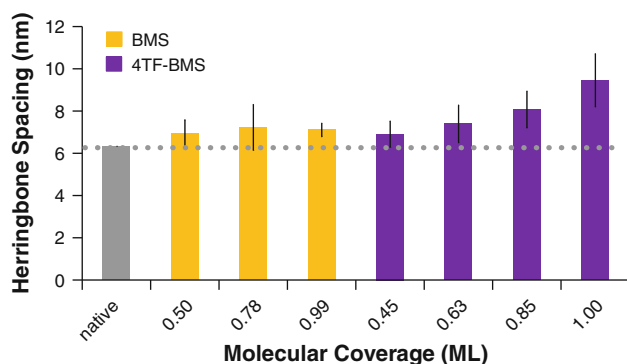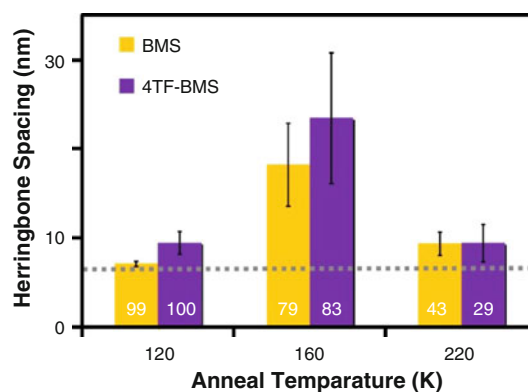

Fig. 8 Plot showing the average herringbone separation as a function of anneal temperature for BMS (*orange*) and 4TF-BMS (*purple*) on Au(111) $(22 \times \sqrt{3})$. The native herringbone reconstruction spacing is indicated by the *dotted grey line*. The initial high coverage systems (120 K) were subsequently annealed to 160 and 220 K. Annealing led to molecular desorption, and molecular coverage (% ML) is indicated by the *white* numbers for each data set. The data from the 120 and 160 K anneals suggest that the lifting of the herringbone reconstruction is a kinetically-limited process, which is aided by an increase in thermal energy. The data from the 220 K anneal reveal that upon desorption of the molecular layer, the Au native reconstruction begins to return

to 220 K leads to significant molecular desorption in both systems, and the herringbone reconstruction begins to return. These observations indicate that the restructuring of the Au surface is a kinetically-limited process, which is accelerated by an increase in thermal energy. These findings are further supported by our previous work examining DBS on Au(111), in which the reversible lifting of the herringbone reconstruction showed a similar temperature dependence [44].

The coverage and temperature-dependent behavior observed in the BMS and 4TF-BMS systems is analogous to that previously reported for DBS on Au(111) [44]. The maximum herringbone separation measured for the system DBS was 11 ± 1 nm (measured for 97% coverage after annealing at 300 K) [44]. We therefore conclude that BMS and 4TF-BMS have a stronger interaction with the Au substrate than DBS, as indicated by the greater degree of surface reorganization exhibited in these systems. A possible rationalization for the observed difference is that the "footprints" for BMS and 4TF-BMS are smaller than that for DBS; consequently, the adsorption of BMS and 4TF-BMS leads to more S–Au bonds per unit area than with DBS and hence more Au surface reorganization. Conversely, both BMS and 4TF-BMS layers are almost fully desorbed after being annealed to 300 K; while DBS was stable with respect to desorption at 300 K. In fact, DBS was present on the surface at a coverage of 0.67 ML even after being annealed to 575 K [44]. The length of the alkyl tails clearly affects the stability of the system. It is likely that longer tails stabilize the molecular layer due to van der

Fig. 7 Plot showing the average herringbone separation for native gold (*grey*) as a function of coverage for BMS (*orange*) and 4TF-BMS (*purple*). Each system was annealed to 120 K. The data suggests that the fluorinated species has a slightly stronger interaction with the Au surface as evidenced by the wider herringbone separations at high coverage
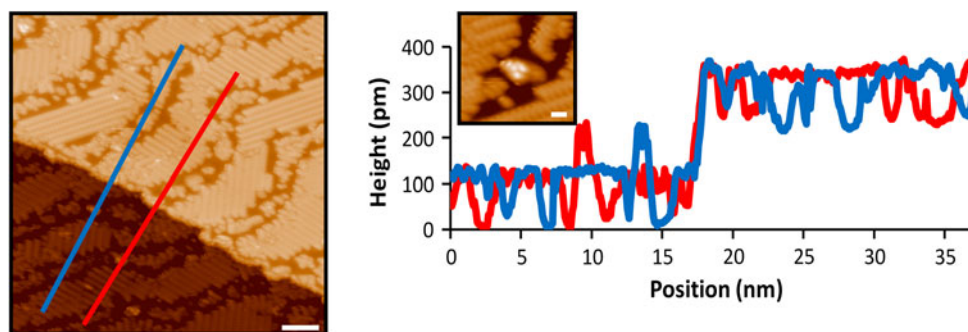
Fig. 9 STM image (*left*) showing 0.73 ML BMS on Au(111) at 78 K after annealing at 120 K. The inset shows a zoomed-in image at an elbow in which three bright lobes are clearly visible. Line scans over the lobes and a step show that they are the same height, suggesting that the lobes are Au atoms. In this system, the herringbone reconstruction is partially lifted; as Au atoms are ejected from the surface, some are trapped at the herringbone elbows. *Scale bar* 5 nm (*inset scale bar* 1 nm). Imaging conditions: 78 K, 200 pA, 200 mV

Waals interactions between the tails in neighboring molecules, as described previously, and between individual molecules and the Au surface. Interestingly, our results indicate that functionalization of the butyl tail does not appear to greatly affect the stability of the molecular layer, as BMS and 4TF-BMS exhibit similar temperature-dependent desorption behavior.

The native herringbone structure of gold is lifted as Au atoms are ejected from the surface layer, and this process often occurs in conjunction with molecular adsorption [23, 64, 66, 67]. If adsorbed species are deposited quickly, the ejected Au adatoms can be trapped near the ejection point [65, 68]. If the molecular layer is not dense, the ejected adatoms can diffuse and incorporate into nearby defects and step edges [69]. Figure 9 shows an STM image taken near a step edge in the medium-coverage BMS system. At this coverage, the herringbone is partially lifted, and most of the Au adatoms diffuse to nearby steps. The low molecular coverage and increased anneal temperature (120 K) provide sufficient space and thermal energy, respectively, for the steps to reorganize (i.e., minimal faceting occurred). However, a small number of Au adatoms are trapped at each elbow and appear as the three-lobed structures in Fig. 9 (see the inset in Fig. 9 for a more detailed image of the three-lobed feature). The edge dislocations at the herringbone elbows serve as the ejection site for Au atoms leaving the surface [70]. Height measurements over step edges and these three-lobed structures confirm that they are the same height as a Au step and are most likely Au atoms (see plot in Fig. 9). We postulate that these three adatoms are complexed with a number of thioether molecules, which stabilize their presence and hinder their diffusion to more stable sites such as step edges.
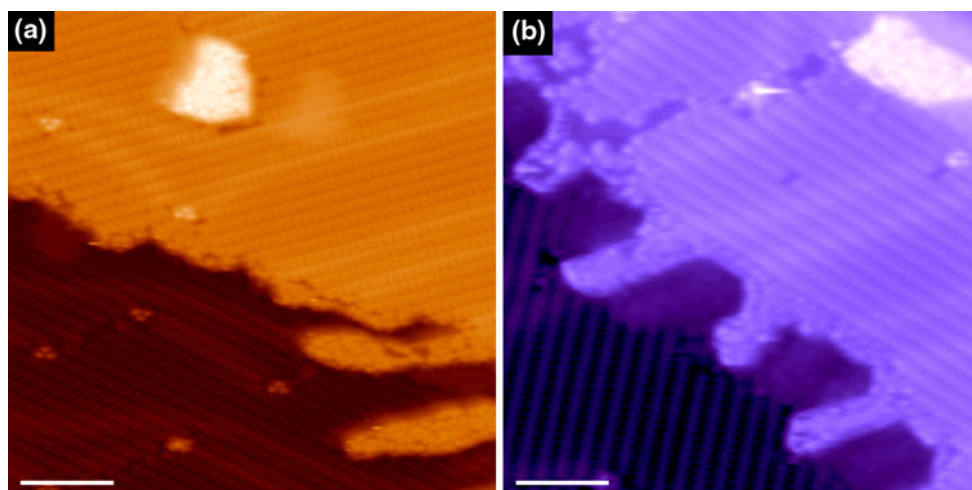

Fig. 10 STM images of **a** 0.99 ML BMS, and **b** 0.99 ML 4TF-BMS on Au(111), both systems have been annealed to 120 K. In these systems, the herringbone reconstruction is partially lifted. Some of the Au atoms ejected from the surface are free to diffuse. These atoms form small islands or combine with step edges to form finger-like extensions. Further reorganization of the surface (i.e., smoothing of the step edge) is hindered due to the dense molecular layer. Other ejected atoms are trapped at elbows (see three-lobed structures) as in the medium-coverage systems. *Scale bars* 5 nm. Imaging conditions: 78 K, **a** 50 pA, 100 mV. **b** 500 pA, −500 mV

The phenomenon of Au atom ejection and incorporation at step edges can also be observed in Fig. 10, which shows STM images taken at step edges of the full coverage BMS and 4TF-BMS systems. These systems differ from that shown in Fig. 9 only in the initial dose, which was higher for those shown in Fig. 10. The full coverage systems contain islands on the terraces and finger-like growths at the step edges, which arise from Au adatoms diffusing to and aggregating with one another at the step edges. The dense molecular layer hinders reorganization of the steps, which leads to the finger-like islands growing from the steps in each system [71]. Also visible are three bright protrusions at the herringbone elbows, which correspond to Au adatoms trapped within the dense molecular layer. These observations support our hypothesis that the lifting of the herringbone reconstruction and Au adatom diffusion is a kinetically-limited process that depends on molecular coverage and temperature.

4 Conclusions

In this report, we have examined the behavior of two asymmetric thioether species adsorbed on Au(111) surfaces as a function of coverage and temperature. Both BMS and 4TF-BMS are achiral in the gas phase, but exhibit chirality upon adsorption to the surface of gold. Even though fluorination introduces a significant dipole moment, both molecules exhibit similar self-assembly to form well-ordered homochiral domains of the same unit cell, which vary in size depending on molecular coverage. At medium coverage, the domains are small, and their boundaries are constrained by the soliton walls of Au's herringbone reconstruction. At high coverage, however, the domains span large areas of the surface and are unaffected by the reconstruction. The fact that the introduction of fluorine fails to perturb the overall assembly scheme suggests that other types of functionalization might also have a minimal impact on domain formation. The ability to fine-tune these overlayers for a specific chemical function will open up new possibilities for the chiral templating of surfaces.

The herringbone reconstruction of the Au substrate also evolves as a function of molecular coverage and temperature. Experiments reveal that both species only partially lift the herringbone reconstruction, indicating intermediate interaction strengths for thioethers on gold, less than that of alkanethiols. We observe that the degree of surface reorganization increases with coverage. Furthermore, adding energy to the system in the form of heat has a marked effect on the herringbone separation, indicating that the lifting of the herringbone reconstruction is a kinetically-limited process at low temperatures.

References

1. Pasteur L (1848) Ann Chim Phys 24:442
2. Haq S, Liu N, Humblot V, Jansen APJ, Raval R (2009) Nat Chem 1:409
3. Lorenzo MO, Baddeley CJ, Muryn C, Raval R (2000) Nature 404:376
4. Lorenzo MO, Haq S, Bertrams T, Murray P, Raval R, Baddeley CJ (1999) J Phys Chem B 103:10661
5. Lorenzo MO, Humblot V, Murray P, Baddeley CJ, Haq S, Raval R (2002) J Catal 205:123
6. Barbosa LAMM, Sautet P (2001) J Am Chem Soc 123:6639
7. Hermse CGM, van Bavel AP, Jansen APJ, Barbosa LAMM, Sautet P, van Santen RA (2004) J Phys Chem B 108:11035
8. Fasel R, Wider J, Quitmann C, Ernst KH, Greber T (2004) Angew Chem Int Ed 43:2853
9. Parschau M, Romer S, Ernst KH (2004) J Am Chem Soc 126:15398
10. Parschau M, Kampen T, Ernst KH (2005) Chem Phys Lett 407:433
11. Kacprzak K, Gawronski J (2001) Synthesis-Stuttgart 7:961
12. France S, Guerin DJ, Miller SJ, Lectka T (2003) Chem Rev 103:2985
13. Zaera F (2008) J Phys Chem C 112:16196
14. Fasel R, Parschau M, Ernst KH (2006) Nature 439:449
15. Fasel R, Parschau M, Ernst KH (2003) Angew Chem Int Ed 42:5178
16. Ernst KH, Kuster Y, Fasel R, McFadden CF, Ellerbeck U (2003) Surf Sci 530:195
17. Stacchiola D, Burkholder L, Tysoe WT (2002) J Am Chem Soc 124:8984
18. Lee I, Zaera F (2005) J Phys Chem B 109:12920
19. Gao F, Wang YL, Li ZJ, Furlong O, Tysoe WT (2008) J Phys Chem C 112:3362
20. Lee I, Zaera F (2006) J Am Chem Soc 128:8890
21. Maksymovych P, Sorescu DC, Dougherty D, Yates JT (2005) J Phys Chem B 109:22463
22. Kautz NA, Kandel SA (2008) J Am Chem Soc 130:6908
23. Nenchev G, Diaconescu B, Hagelberg F, Pohl K (2009) Phys Rev B 80:081401
24. Lavrich DJ, Wetterer SM, Bernasek SL, Scoles G (1998) J Phys Chem B 102:3456
25. Weidner T, Ballav N, Siemeling U, Troegel D, Walter T, Tacke R, Castner DG, Zharnikov M (2009) J Phys Chem C 113:19609
26. Santagata NM, Lakhani AM, Davis BF, Luo PS, Nardelli MB, Pearl TP (2010) J Phys Chem C 114:8917
27. Lakhani AM, DeWitt DJ, Sant'Agata NM, Pearl TP (2007) J Phys Chem C 111:5750
28. Xiao WD, Jiang YH, Aiet-Mansour K, Ruffieux P, Gao HJ, Fasel R (2010) J Phys Chem C 114:6646
29. Bombis C, Weigelt S, Knudsen MM, Norgaard M, Busse C, Laegsgaard E, Besenbacher F, Gothelf KV, Linderoth TR (2010) ACS Nano 4:297
30. Bartels L (2010) Nat Chem 2:87
31. Barth JV, Weckesser J, Trimarchi G, Vladimirova M, De Vita A, Cai CZ, Brune H, Gunter P, Kern K (2002) J Am Chem Soc 124:7991

32. Bohringer M, Morgenstern K, Schneider WD, Berndt R, Mauri F, De Vita A, Car R (1999) Phys Rev Lett 83:324
33. Bohringer M, Schneider WD, Berndt R (2000) Angew Chem Int Ed 39:792
34. De Feyter S, Gesquiere A, Wurst K, Amabilino DB, Veciana J, De Schryver FC (2001) Angew Chem Int Ed 40:3217
35. Cortes R, Mascaraque A, Schmidt-Weber P, Dil H, Kampen TU, Horn K (2008) Nano Letters 8:4162
36. Chen Q, Richardson NV (2003) Nat Mater 2:324
37. Forster M, Dyer MS, Persson M, Raval R (2010) Angew Chem Int Ed 49:2344
38. Kuhnle A, Linderoth TR, Hammer B, Besenbacher F (2002) Nature 415:891
39. Patole SN, Baddeley CJ, Schuler A, O'Hagan D, Richardson NV (2009) Langmuir 25:1412
40. Parschau M, Passerone D, Rieder KH, Hug HJ, Ernst KH (2009) Angew Chem Int Ed 48:4065
41. Mark AG, Forster M, Raval R (2010) Tetrahedron-Asymmetry 21:1125
42. Jensen SC, Baber AE, Tierney HL, Sykes ECH (2007) ACS Nano 1:423
43. Jensen SC, Baber AE, Tierney HL, Sykes ECH (2007) ACS Nano 1:22
44. Bellisario DO, Jewell AD, Tierney HL, Baber AE, Sykes ECH (2010) J Phys Chem C 114:14583
45. Tierney HL, Calderon CE, Baber AE, Sykes ECH, Wang F (2010) J Phys Chem C 114:3152
46. Tierney HL, Jewell AD, Baber AE, Iski EV, Sykes ECH (2010) Langmuir 26:15350
47. Baber AE, Tierney HL, Sykes ECH (2008) ACS Nano 2:2385
48. Bellisario DO, Baber AE, Tierney HL, Sykes ECH (2009) J Phys Chem C 113:5895
49. Noh J, Kato HS, Kawai M, Hara M (2002) J Phys Chem B 106:13268
50. Noh J, Murase T, Nakajima K, Lee H, Hara M (2000) J Phys Chem B 104:7411
51. Noh J, Nakamura F, Kim J, Lee H, Hara M (2002) Mol Cryst Liq Cryst 377:165
52. Jewell AD, Tierney HL, Baber AE, Iski EV, Laha MM, Sykes ECH (2010) J Phys-Condens Mater 22:264006
53. Burgi L, Brune H, Kern K (2002) Phys Rev Lett 89:176801
54. Rzeznicka II, Lee JS, Maksymovych P, Yates JT (2005) J Phys Chem B 109:15992
55. Baber AE, Jensen SC, Sykes ECH (2007) J Am Chem Soc 129:6368
56. Bohringer M, Morgenstern K, Schneider WD, Wuhn M, Woll C, Berndt R (2000) Surf Sci 444:199
57. Sykes ECH, Mantooth BA, Han P, Donhauser ZJ, Weiss PS (2005) J Am Chem Soc 127:7255
58. Jewell AD, John-Rajkumar SV, Rabinovich D, Sykes ECH (under review)
59. Tierney HL, Han JW, Jewell AD, Iski EV, Baber AE, Sholl DS, Sykes ECH (2011) J Phys Chem C 115:897
60. Müller U (1993) Inorganic structural chemistry. Wiley, West Sussex
61. Tierney HL, Baber AE, Jewell AD, Iski EV, Boucher MB, Sykes ECH (2009) Chem-Eur J 15:9678
62. Tierney HL, Baber AE, Sykes ECH, Akimov A, Kolomeisky AB (2009) J Phys Chem C 113:10913
63. Syomin D, Kim J, Koel BE, Ellison GB (2001) J Phys Chem B 105:8387
64. Maksymovych P, Sorescu DC, Yates JT (2006) Phys Rev Lett 97:146103
65. Jewell AD, Tierney HL, Sykes ECH (2010) Phys Rev B 82:205401
66. Taylor R, Torr N, Huang Z, Li FS, Guo QM (2010) Surf Sci 604:165
67. Min BK, Alemozafar AR, Biener MM, Biener J, Friend CM (2005) Top Catal 36:77
68. Driver SM, Zhang TF, King DA (2007) Angew Chem Int Ed 46:700
69. Biener MM, Biener J, Friend CM (2007) Surf Sci 601:1659
70. Meyer JA, Baikie ID, Kopatzki E, Behm RJ (1996) Surf Sci 365:L647
71. Guo QM, Yin F, Palmer RE (2005) Small 1:76